High-order simulation scheme for active particles driven by stress boundary conditions

B Deußen[1] , A Jayaram[2] , F Kummer[1] , Y Wang[1] , T Speck[2] and M Oberlack[1,*]

[1] Chair of Fluid Dynamics, Department of Mechanical Engineering, Technical University of Darmstadt, Germany
[2] Institute of Physics, Johannes Gutenberg-University Mainz, Germany

E-mail: oberlack@fdy.tu-darmstadt.de

CrossMark

Abstract

We study the dynamics and interactions of elliptic active particles in a two dimensional solvent. The particles are self-propelled through prescribing a fluid stress at one half of the fluid-particle boundary. The fluid is treated explicitly solving the Stokes equation through a discontinuous Galerkin scheme, which allows to simulate strictly incompressible fluids. We present numerical results for a single particle and give an outlook on how to treat suspensions of interacting active particles.

Keywords: active matter, hydrodynamic interactions, microswimmers, discontinuous Galerkin, computational fluid dynamics

(Some figures may appear in colour only in the online journal)

1. Introduction

Motile organisms like bacteria and sperm cells have to generate directed motion in an aqueous environment at low Reynolds numbers [1, 2]. The time-reversibility of the governing Stokes equation requires flagella beats or body deformation cycles that break symmetry [3]. Synthetic microswimmers have been designed that mimic this motion [4, 5]. However, even without movable parts, 'swimming' at the microscale is possible through phoretic mechanisms that maintain a stress in the fluid boundary layer driving a large-scale flow that propels the particle forward. Typically, these are colloidal Janus particles with two chemically distinct hemispheres [6, 7], but also the exchange of ions with different diffusion coefficients [8] or a difference of surface tension can be exploited [9].

Most numerical studies of active particles [10], however, neglect hydrodynamic interactions or employ simplified, schematic models such as Lighthill's squirmers [11]. These models do not resolve fluid details between the moving particles but typically prescribe a solvent velocity at the particle boundary, and the solvent is treated using mesoscopic methods like the *lattice-Boltzmann method* [12] or *multiparticle collision dynamics* [13, 14] (note the boundary integral method [15] as an alternative). While these methods conserve momentum and thus hydrodynamic far-field flow, they are limited in their resolution of near-field interactions due to the finite grid underlying the fluid-particle collision interactions. Moreover, the simulated fluid is compressible and care has to be taken to avoid artifacts due to density inhomogeneities [16]. Another aspect is that the concept of a slip velocity is questionable from a thermodynamic point of view [17, 18]. It is thus highly desirable to explore the collective behavior of active particles both in a strictly incompressible fluid and employing different types of boundary conditions.

The present work investigates active particle motion in an Newtonian solvent on an essentially two-dimensional

* Author to whom any correspondence should be addressed.

manifold. The reason is that the major bulk of experimental (and also numerical) work on active matter has been performed in (quasi) two-dimensional geometries. Due to low Reynolds numbers, the Stokes equation governs the flow dynamics of the soluble medium. It is well known that there exists no steady-state solution for the Stokes equation describing a free flow around a disk in two dimensions (or around an infinitely long cylinder) if the no-slip condition on the cylinder surface and the free flow condition at infinity have to be satisfied simultaneously. If at infinity only a relaxed asymptotic boundary condition is required, the Stokes equation can yield a very reasonable solution in the near field, while in the far field the prerequisite of a Stokes flow will no longer be met. This phenomenon is called Stokes' paradox. However, the improvement by the Oseen correction, obtained by the perturbation method, is necessary only in the far field $r/a > \mathcal{O}(\mathrm{Re}^{-1})$ with the cylinder radius a, which in our case would result in $r > 100 \times \text{particle} - \text{length}$ for $\mathrm{Re} = \mathcal{O}(10^{-2})$. This exceeds the size of the domain we consider. Furthermore, it will be seen that the fluid velocity obtained in the present investigation decays as $1/r^2$ with the distance r from the particle, hence the fluid velocity in the far field would be 10^{-4} times smaller than the particle velocity. In real systems such small velocity will be overlaid by noise and are negligible. Therefore, in the present investigation with a Reynolds number of $\mathrm{Re} = \mathcal{O}(10^{-2})$, a two-dimensional Stokes flow solution is reliable.

Here we present a detailed numerical study solving the underlying Stokes equation using a high-order extended discontinuous Galerkin (DG) discretization scheme [19]. This method provides a sharp interface representation between the fluid and the particle phase [20]. Besides the ability to use higher order, DG-methods have additional advantages, for example a simple handling of hanging nodes and thus local mesh refinements, due to the discontinuous approach at the cell boundaries. The fluid-particle solver used in this work is part of the bounded support spectral solver[3] (BoSSS) framework [21], which contains all underlying methods. In contrast to mesoscopic fluid solvers, such a method allows to accurately resolve boundary conditions. We exploit this advantage and implement the stress boundary condition proposed by Shelley and coworkers [22, 23], which is physically more reasonable for the representation of the forcing of active particles, but has received comparably little attention as an alternative to slip boundary conditions. The particle shape is chosen to be elliptic [16, 24].

2. Model

For the moment we consider N active elliptic particles suspended in a fluid. At each point **x** there is either a particle or the fluid present. Hence, the two-dimensional domain Ω splits into a sub-domain Ω_f occupied by the fluid and $\Omega_s = \bigcup_{p=1}^{N} \Omega_p$ occupied by the particles. Both phases are separated by the interface $\Gamma = \bigcup_{p=1}^{N} \Gamma_p$, which consists of the individual particle surfaces Γ_p. The coordinate system is defined by the two
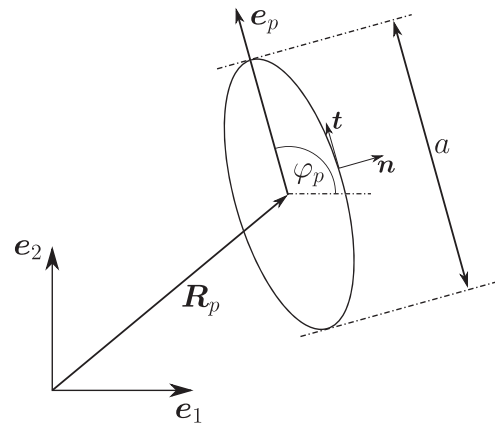
Figure 1. Each particle is defined by the two variables $\mathbf{R}_p$, which is the position of the centre of mass and the orientation angle φ_p. The angle is defined between the horizontal axis with the unit vector $\mathbf{e}_1$ and the orientation vector $\mathbf{e}_p$. The normal vector $\mathbf{n}$ and the tangential vector $\mathbf{t}$ form a right-handed system. The length of the particle is denoted by a.

unit vectors $\mathbf{e}_1$ and $\mathbf{e}_2$. A third unit vector $\mathbf{e}_3$ is defined normal to the $\mathbf{e}_1$–$\mathbf{e}_2$ plane.

The state of each particle is defined by the position of its centre of mass $\mathbf{R}_p$, the orientation angle φ_p and their time derivatives. The orientation vector is $\mathbf{e}_p \equiv (\cos \varphi_p, \sin \varphi_p)$ (cf figure 1). The particles are considered to be rigid. Hence, their translational and rotational motion is described by the Newton–Euler equations

$$m_p \ddot{\mathbf{R}}_p = F_p = \int_{\Gamma_p} \boldsymbol{\tau} \cdot \mathbf{n} \, \mathrm{d}S \qquad (1)$$

and

$$I_p \ddot{\varphi}_p = T_p = \int_{\Gamma_p} (\mathbf{x} - \mathbf{R}_p) \times (\boldsymbol{\tau} \cdot \mathbf{n}) \cdot \mathbf{e}_3 \, \mathrm{d}S, \qquad (2)$$

where $\mathbf{F}_p$ is the hydrodynamic force vector and T_p the hydrodynamic torque exerted on the particle p. The resulting linear and angular accelerations of the particle are determined by its mass m_p and moment of inertia I_p (which is a scalar quantity due to the restriction to two dimensions).

To calculate the hydrodynamic forces, we need to know the fluid stress tensor

$$\boldsymbol{\tau} = -p\boldsymbol{I} + \mu_\mathrm{f} \left[\nabla \mathbf{u} + (\nabla \mathbf{u})^\mathrm{T} \right], \qquad (3)$$

where $\boldsymbol{I}$ is the identity matrix, μ_f the solvent viscosity, and $\mathbf{u}(\mathbf{x}, t)$ the fluid velocity field in the vicinity of the particle. As appropriate for motion at low Reynolds number, the evolution of the fluid is governed by the unsteady Stokes equation

$$\rho_\mathrm{f} \frac{\partial \mathbf{u}}{\partial t} = \nabla \cdot \boldsymbol{\tau} = -\nabla p + \mu_\mathrm{f} \Delta \mathbf{u}, \qquad (4)$$

where ρ_f is the fluid density and the pressure field $p(\mathbf{x}, t)$ ensures incompressibility,

$$\nabla \cdot \mathbf{u} = 0. \qquad (5)$$

To complete the model, we need to specify boundary conditions between the particles and the fluid. The particles are
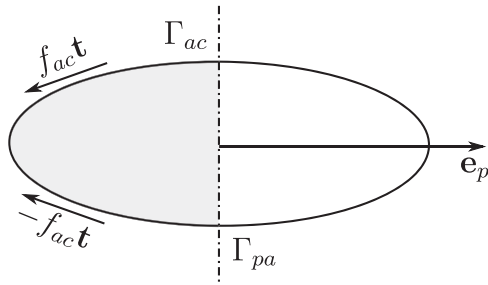
Figure 2. Sketch of an elliptic Janus pusher particle. On the active part of the particle's surface, the fluid is accelerated by the tangential stress $\pm f_{ac}\boldsymbol{t}$. Due to momentum conservation, the particle will move in the direction of $\mathbf{e}_p$. At the passive half of the particle surface, a no-slip boundary condition is applied.

modelled as elliptic Janus particles with each hemiellipse (denoted Γ_{ac} for the active side and Γ_{pa} for the passive side, see figure 2) described by a different boundary condition. By prescribing a stress vector along the tangential direction on the active surface, the fluid is accelerated and the particle moves in the opposite direction. The dynamic stress vector on the unit surface of an infinitesimal fluid element is

$$\mathbf{s}_d = \mu_f \left(\nabla \mathbf{u} + (\nabla \mathbf{u})^\mathrm{T} \right) \cdot \mathbf{n}, \tag{6}$$

where $\mathbf{n}$ is the vector normal to the surface. On the active surface, the tangential part of the dynamic stress vector is prescribed to be

$$\mathbf{t} \cdot \mathbf{s}_d = \pm f_{ac} \quad \text{on } \Gamma_{ac}, \tag{7}$$

where $\mathbf{t}$ is the tangential vector and f_{ac} is the specified magnitude of the active stress. For symmetry reasons, the sign of f_{ac} is different on the two halves of the active hemiellipse (see figure 2). Furthermore, the sign determines whether the particle is a 'pusher' or a 'puller'. In figure 2, a pusher particle is shown. For a puller, the active stress would have the opposite sign.

The local particle velocity consists of the translational velocity $\dot{\mathbf{R}}_p$ and the rotational velocity $\dot{\varphi}$

$$\mathbf{u}_p = \dot{\mathbf{R}}_p + \dot{\varphi}_p \mathbf{e}_3 \times \left(\mathbf{x} - \mathbf{R}_p \right) \quad \forall \, \mathbf{x} \in \Omega_p. \tag{8}$$

The additional active stress admits a slip velocity at the surface

$$\left(\mathbf{u} - \mathbf{u}_p \right) \cdot \mathbf{t} \neq 0 \quad \forall \, \mathbf{x} \in \Gamma_{ac}. \tag{9}$$

Since the surface is considered to be impenetrable, along the normal direction, the fluid and particle velocity at the active boundary have to be equal. Hence, the normal boundary condition on the active part of the particle surface is

$$\mathbf{u} \cdot \mathbf{n} = \mathbf{u}_p \cdot \mathbf{n} \quad \forall \, \mathbf{x} \in \Gamma_{ac}. \tag{10}$$

Finally, on the passive part of the particle surface, a no-slip boundary condition

$$\mathbf{u} = \mathbf{u}_p \quad \text{on } \forall \, \mathbf{x} \in \Gamma_{pa} \tag{11}$$

is used.

3. Results

The solution for a system of *N* particles and a fluid is obtained with a separated solver. Due to the interdependence of the two phases, an iterative procedure is necessary. First, the solution for the fluid phase is obtained by solving the unsteady Stokes equation (4) and the continuity equation (5) in the fluid domain Ω_f. At the particle's surface Γ, the solution of the particles from the previous iteration is used to define the boundary conditions (7), (10) and (11). A high order extended discontinuous Galerkin (XDG) method is employed, extending the work of [19, 20]. The acceleration, and subsequently the new velocity, position and orientation of the particles are obtained by solving the Newton–Euler equations (1) and (2) using the solution of the fluid phase. The new state of the particle is then used in the next iteration until a 'steady' result for the particle velocities is obtained. In appendix A, we provide further details on the implementation of the numerics.

In every simulation presented in the following subsections, the fluid properties density ρ_f and viscosity μ_f and the particle length *a* are set to unity thereby fixing the ratio between the length and time scales. Hence, the Reynolds number $\mathrm{Re} = \frac{\rho_f u_p a}{\mu_f}$ is solely governed by the aspect ratio ϵ and the active stress f_{ac}, which in turn sets the velocity u_p of the particle. To justify the usage of the unsteady Stokes equation over the Navier–Stokes equation, the Reynolds number has to be kept small, i.e. $\mathrm{Re} \ll 1$.

3.1. Single particle characteristics

In this section, we will examine the behaviour of a single particle to outline certain characteristics. A single active particle generates the flow field of a force dipole [25], which is visible in the experiments of the aforementioned publication and in the results of our numerical simulation (see figure 3). To reproduce the results of the experiment, we use a 10×10 domain with an active particle in the centre. The domain is moved alongside the particle, hence it always stays in the centre. The particle has an aspect ratio of $\varepsilon = 0.1$. The boundary condition at the domain boundary is a pressure outflow. Hence, there are no walls to disturb the motion of the particle.

Comparing our simulation results with the experimental results of reference [25] demonstrates that our simulations correctly reproduce the qualitative behaviour. Both data sets show the symmetric velocity field of a force dipole in the far field (see figure 4(a)). In the region close to the particle's surface, the shape of the flow field deviates from a force dipole (see figure 4(b)). At the posterior side of the particle, a minimum exists at $r \approx 4 \times 10^{-1}$, where r is the distance from the surface. This minimum is caused by the opposing signs of the slip velocity generated by the active stress on the upper and lower sides of the active surface. Plotting the velocity perpendicular to the particle's surface at the point where the active and passive boundaries connect reveals further interesting effects. Close to the boundary, the fluid speed has a minimum, i.e., a stagnation point is generated. At a slightly greater distance from the surface, the speed increases to a maximum, which is caused by the active boundary which pulls additional fluid.
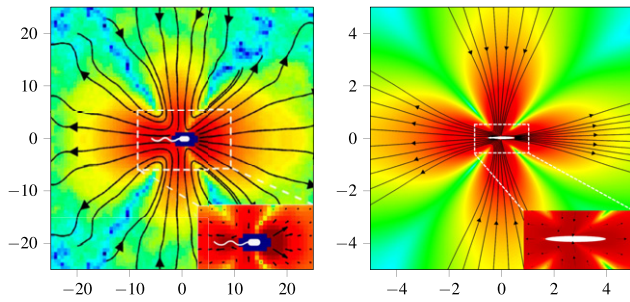
Figure 3. Qualitative comparison between three-dimensional experimental results [25] of the (rotationally symmetric) flow field of *Escherichia coli* (left, copyright 2011 National Academy of Sciences) and our two-dimensional numerical results obtained with BoSSS (right). The colour show the magnitude of the fluid velocity. In the far field region, the flow field of a force dipole is retrieved. In the region close to the particle's surface, the flow field shows an asymmetry caused by the different boundary conditions. This asymmetry is also visible in the close-up picture of the experimental results.
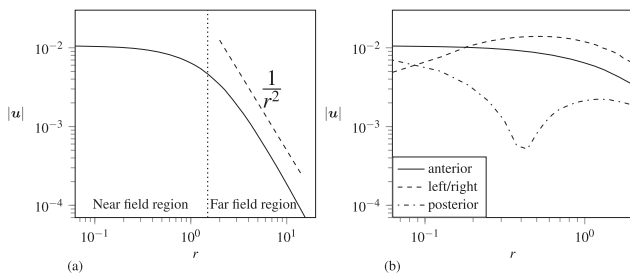

Figure 4. (a) Line-out plot of the fluid speed $|\mathbf{u}|$ at the anterior side of the particle. In the far field region, the value decays as $|\mathbf{u}| \sim \frac{1}{r^2}$, which is equivalent to a force dipole. (b) Line-out plots of the fluid speed at the different sides of a pusher particle's surface in the near-field region. There is no minimum at the anterior side, whereas on the posterior side a minimum occurs due to the different signs of the slip velocity alongside the surface. On the left and right side of the particle a minimum in the fluid speed occurs where the two different boundary conditions coincide.

Increasing the distance even further will lead to the transition layer between the near- and far-field.

In a first parameter study, a particle is set in a closed domain, i.e., with solid wall boundary conditions. The domain has a size of 5×5 with 60 cells in both spatial directions. A moving domain ensures the particle is always positioned at the center of the domain. The particle length is unity and the aspect ratio $\varepsilon = 0.5$. Only the magnitude of the active stress is varied. The resulting normalized speed of the particle

$$v = \frac{|\dot{\mathbf{R}}|}{|\dot{\mathbf{R}}|_{\max}} \tag{12}$$

is plotted in figure 5 over the active stress, where $|\dot{\mathbf{R}}|_{\max}$ is the terminal speed of the simulation with the largest magnitude of the active stress. In alignment with the results of the theoretical examinations [26], the speed of the particle is proportional to the magnitude of the active stress. This result is to be expected. Since the Stokes equation, the Newton equation, and all boundary conditions are linear in both the fluid velocity and
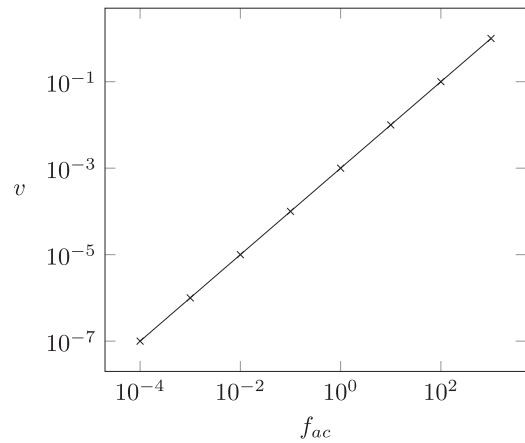

Figure 5. Particle speed v as function of the active stress f_{ac}, where the results of eight simulations are marked with ($\times$). The speed is normalized with the maximum value, $v = |\dot{\mathbf{R}}|/|\dot{\mathbf{R}}|_{\max}$.

the particle fluid, and f_{ac} is the only forcing, the fluid velocity and the particle speed are proportional to f_{ac}. Therefore, in the present special case the forcing f_{ac} can be removed from the problem statement by an appropriate non-dimensionalization. Introducing the translational mobility σ_{t} as a proportionality factor yields

$$\left|\dot{\mathbf{R}}\right| = \sigma_{\mathrm{t}} f_{\mathrm{ac}}, \tag{13}$$

which is found to be $\sigma_{\mathrm{t}} \simeq 5.952$.

The setup of the second parameter study is similar to the first one. However, the parameter in question is the aspect ratio of the particle. While the length a of the particle in the horizontal direction is kept at unity, the thickness b in the vertical direction is varied. In figure 6, we plot the terminal speed over the aspect ratio of the particle. For small aspect ratios $\varepsilon < 0.325$ our numerical results approach a logarithmic behavior, which is in line with the predictions of slender body theory [27]. For values in between $0.325 < \varepsilon < 0.6$ our results match the theoretical prediction of Hohenegger and Shelley [26]. After the minimum of $\varepsilon|\ln(\varepsilon^2) + 1|$, our values return to a logarithmic behaviour. The theory of Hohenegger and coworkers approximates the integrated value of the active stress, i.e. the active force, by $2\pi b f_{\mathrm{ac}}$, which is a zeroth order approximation of the surface of an ellipse multiplied with the magnitude of the active stress. Hence, the theory predicts a shrinking velocity for smaller aspect ratios ε. In contrast, BoSSS resolves the shape in greater detail and calculates the active force by the surface integral accurately over the entire surface of the active hemiellipse, leading to a further increase of the velocity for small ε.

3.2. Single particle in a channel

In this section, we present the fundamentally different behaviour of a puller and a pusher particle. In both cases the particle is initially set in the center of a 7.5×1.5 channel domain with walls at the upper and lower side and a pressure Dirichlet boundary condition at the left respective right side of the domain. The aspect ratio of each particle is $\varepsilon = \frac{1}{3}$. For the pusher particle the active stress is applied at the posterior
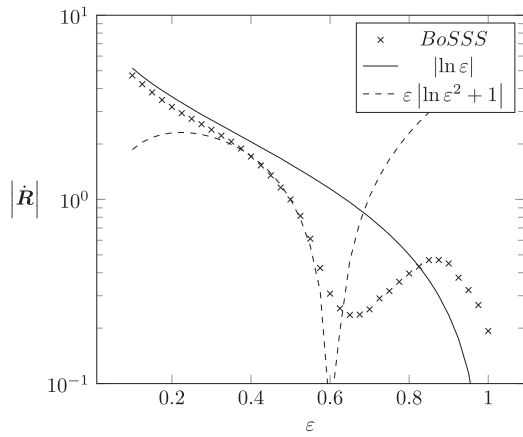
Figure 6. The diagram shows the speed of the particle v over the aspect ratio of the active particle $\varepsilon < 1$. The results of the simulations are marked by (x). For smaller ε the results align towards a logarithmic function of ε. For a medium range of ε, the theoretical result of Hohenegger and Shelley [26] (dashed line) is in good agreement with our numerical results.

Figure 7. A puller particle in a channel at $t = 0$ and $t = 5$ with $\Delta t = 10^{-2}$, where the colour scale indicates the magnitude of the fluid velocity. The particle aligns itself parallel to the channel walls in the middle of the channel.
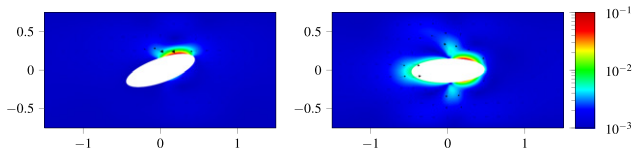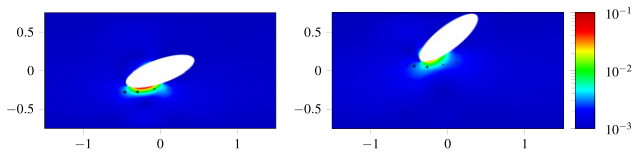

Figure 8. A pusher particle in a channel at $t = 0$ and $t = 10$ with $\Delta t = 10^{-2}$, where the colour scale indicates the magnitude of the fluid velocity. The particle continuously approaches the channel wall.

side, whereas, for the puller particle the active stress is applied on the anterior side. Both particles are tilted by an angle of $\varphi_p = \frac{\pi}{9}$ with respect to the horizontal axis. The puller particle aligns itself parallel to the walls in the middle of the channel, see figure 7. This behaviour is stable and the angle approaches

$$\lim_{t \to \infty} \varphi_{\mathrm{pull}} = 0. \tag{14}$$

The pusher particle, on the other hand, shows a different behaviour, see figure 8. In the first section of the simulation, the angle increases to $\varphi = \frac{\pi}{4}$ while the particle steadily moves closer to the channel's wall. Once the particle reaches the wall region its speed decreases and it stays close to the wall. Such alignment of pushers at walls of a confinement in two dimensions has been observed, for e.g., in references [28, 29].
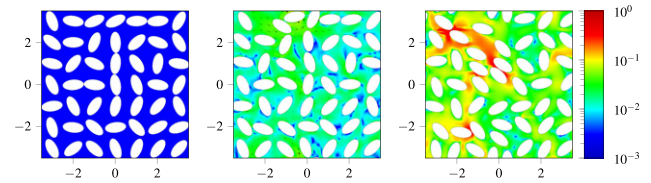

Figure 9. The three snapshots show the progress of a simulation with 49 active particles at $t = 0$, $t = 7.5$ and $t = 15$. The time step $\Delta t = 10^{-1}$ and the Reynolds number is in the order of $\mathcal{O}(\mathrm{Re}) = 10^{-2}$. The colour field is the fluid speed and the arrows represent the fluid velocity field.
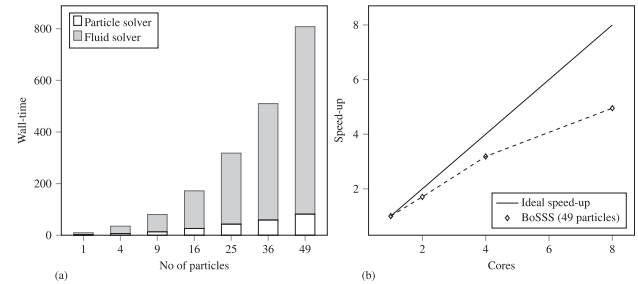

Figure 10. (a) Wall-time in seconds to compute a single time-step on a single core of a system with a constant volume fraction of the particles of 39.42%. There is one particle for each 540 DoF in the fluid phase and the polynomial degree is $k = 2$. (b) Speed-up for the largest system in (a) with 49 particles.

3.3. Active suspension

Finally, we give a brief glimpse of suspensions on active particles. Figure 9 shows snapshots of $N = 49$ particles with an aspect ratio $\varepsilon = 0.5$ in a 7×7 domain with periodic boundaries. This results in an area fraction occupied by the particles of 39.42%. The boundary conditions on the particles induce a highly non-trivial fluid velocity. These simulations will be analyzed in detail in forthcoming publications.

Results of wall-time measurements are displayed in figure 10. We use a direct sparse solver PARDISO [30] for the fluid domain, which is expected to out-perform iterative solvers for small systems with less than 10^5 degrees of freedom (DoF) in the fluid phase [21]. All calculations for this performance test are carried out on a desktop machine with an Intel(R) Core(TM) i7-9700K. Tests on a single core with an increasing number of particles and fluid-DoFs deliver the behaviour shown in diagram (a) in figure 10. The main contributor to the run-time is the fluid solver, including the assembly of the matrix, the handling of cut-cells, quadrature rules and the calls to PARDISO. The particle solver contributes with about 10% to the overall run-time. The main source from the particle solver is the integration of the fluid stress tensor at the surface to obtain hydrodynamic forces and torque. Tests for a system on multiple cores with 49 particles and 26 460 DoFs in the fluid deliver the speed-up visualized in diagram (b) in figure 10.

4. Conclusions

We have demonstrated for the first time that DG methods are a viable alternative to study the dynamics of self-propelled active particles in an explicit, strictly incompressible solvent. Going beyond existing studies, instead of prescribing a solvent speed at the particles' boundary we have used a stress boundary condition. We have discussed the technical details of the implementation and studied numerically the dynamics of a single active particles in two geometries, a free particle and a particle moving in a channel. We find good agreement with experiments [25] and previous theoretical calculations [26]. Our approach can be extended to suspensions of interacting particles, which will be studied in more detail elsewhere.

Acknowledgments

Data availability statement

The data that support the findings of this study are available upon reasonable request from the authors.

Appendix A. Implementation details

For completeness, here we describe in some detail the implementation within BoSSS. The system of the fluid and N particles is coupled at the particle surface due to the boundary conditions (7), (10), (11) and the Newton–Euler equations (1) and (2). To represent the particle surface a level-set function ϕ is used. This level-set is solely a function of the position of the centre of mass and the orientation angle

$$\phi = \phi(\chi, \varphi), \tag{A.1}$$

thus, no additional level-set equation is necessary. Furthermore, to reduce the number of independent level-set function a complete level-set function ϕ is introduced

$$\phi(\mathbf{x}, t) = \inf(\Phi(\mathbf{x}, t)), \tag{A.2}$$

where

$$\Phi(\mathbf{x}, t) = \{\phi_1(\mathbf{x}, t), \phi_2(\mathbf{x}, t), \dots, \phi_N(\mathbf{x}, t)\}. \tag{A.3}$$

The total time T is divided into separate time steps Δt. The state of the fluid at each time step is represented by

$$\mathbf{U}^n(\mathbf{x}) = \begin{bmatrix} \mathbf{u}^n(\mathbf{x}) \\ p^n(\mathbf{x}) \end{bmatrix} \tag{A.4}$$

and the state of each particle is

$$\mathbf{V}^n = \begin{bmatrix} \mathbf{R}_p^n \\ \dot{\mathbf{R}}_p^n \\ \varphi_p^n \\ \dot{\varphi}_p^n \end{bmatrix}. \tag{A.5}$$

Note that the particle state does not depend on the position $\mathbf{x}$. Due to the coupling between fluid and particle phase the fluid state at a new time step t^{n+1} is calculated with

$$\mathbf{U}^{n+1} = \mathcal{F}\left(\mathbf{U}^n, \mathbf{U}^{n-1}, \dots \mathbf{U}^{n-a}; \mathbf{V}_1^{n+1}, \dots\right.$$
$$\left. \mathbf{V}_N^{n+1}, \mathbf{V}_1^n, \dots \mathbf{V}_N^n, \dots \mathbf{V}_1^{n-a}, \dots \mathbf{V}_N^{n-a}\right), \tag{A.6}$$

where $\mathcal{F}$ is the fluid solver scheme, to be defined in the following sections. As shown in (A.6), the new state depends not only on the previous states of the fluid but also on the current and previous states of the particles. The number of previous states a necessary depends on the temporal discretization scheme, introduced in section appendix A.1.

To obtain the new state of the particle phase it is necessary to consider the history of the respective particle and the current state of the fluid. Hence, one obtains

$$\mathbf{V}^{n+1} = \mathcal{P}\left(\mathbf{U}^{n+1}; \mathbf{V}^n, \dots \mathbf{V}^{n-a}\right), \tag{A.7}$$

where $\mathcal{P}$ is the particle solver scheme.

Due to the dependency of both phases on the current state of the respective other phase it is necessary to employ either a combined solver or an iterative, separated solver. The iteration scheme is shown in figure A1. In each iteration marked with the preceding index k the fluid and the particle solver are employed separately. Starting with the fluid solver the velocity and pressure fields are calculated. The results are then used to calculate the hydrodynamic forces and torque in the Newton–Euler equations (1) and (2) and subsequently the translational and rotational velocity of each particle. The newly obtain particle velocities are then used to update the boundary conditions at the particle surface (7), (10) and (11) and to obtain a new solution for the fluid velocity and pressure. This procedure is repeated until the residual $\mathcal{R}$ has fallen below a critical value $\mathcal{R}_{\mathrm{crit}}$. The residual is calculated with the hydrodynamic forces and torque acting on all particles

$$\mathcal{R} = \sqrt{\frac{\sum_{p=1}^N \left(k+1|\mathbf{F}|^{n+1} - k|\mathbf{F}|^{n+1}\right)^2}{\sum_{p=1}^N \left(k+1|\mathbf{F}|^{n+1}\right)^2}}, \tag{A.8}$$

where the vector $\mathbf{F}$ contains both the vector of the hydrodynamic forces and torque

$$\mathbf{F} = \left[\mathbf{F}_p, T_p\right]. \tag{A.9}$$

After the velocities of both phases and the pressure has been determined it is checked whether the particles would collide or even overlap with the new velocities within the current time step. In this case a collision procedure, based on the momentum and energy conservation principle, is applied. With the
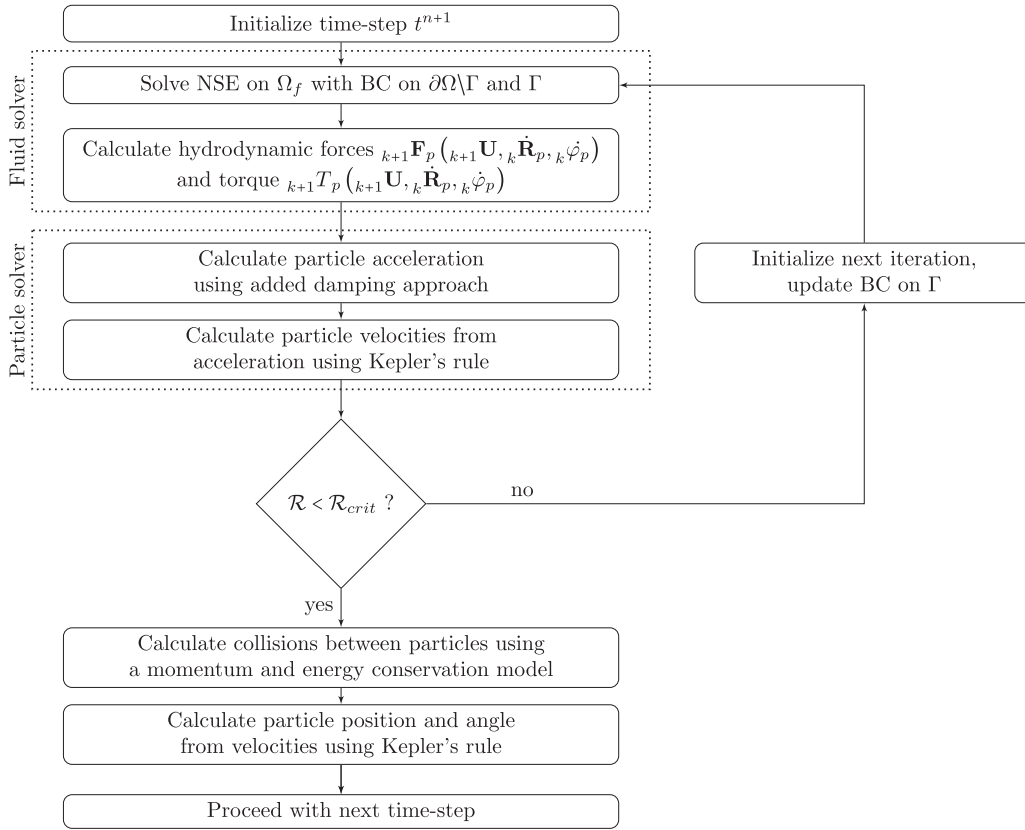
Figure A1. Schematic representation of the coupled two-phase solver. The residual R is calculated using (A.8). The criterion $\mathcal{R}_{\text{crit}} \ll 1$ is set at a reasonable value at the beginning of the simulation.

new velocities and pressure and the determination of eventual collisions the position χ and angle φ of all particles are updated. The level-set ϕ used to describe the particle surface is then updated for the next time step.

A.1. Temporal discretization

To discretize the fluid in time a backward differencing formula of second order (BDF2) is used [20], whereas for the particle phase Kepler's rule is used. Note, that the time steps Δt do not necessarily be uniform. After the extrapolation in time (4) becomes

$$
\rho_{\text{f}} \left(\frac{3\mathbf{u}^{n+1}}{2\Delta t} - \frac{2\mathbf{u}^{n^*}}{\Delta t} + \frac{\mathbf{u}^{n-1^*}}{\Delta t} \right) \\
+ \nabla p^{n+1} - \mu_{\text{f}} \Delta \mathbf{u}^{n+1} = 0 \quad \text{in } \Omega_{\text{f}} \left(t^{n+1} \right).
$$
(A.10)

The continuity equation (5) becomes

$$
\nabla \cdot \mathbf{u}^{n+1} = 0 \quad \text{in } \Omega_{\text{f}} \left(t^{n+1} \right).
$$
(A.11)

The fluid domain Ω_{f} depends on the time step, hence, the velocity fields $\mathbf{u}^{n^*}$ and $\mathbf{u}^{n-1^*}$ occurring in (A.10) are unknown. However, it is assumed that the change from $\Omega_{\text{f}}(t^n)$ to $\Omega_{\text{f}}\left(t^{n+1}\right)$ is small and thus, it is possible to use

$$
\mathbf{u}^{n^*} = \mathbf{u}^n \quad \text{in } \Omega_{\text{f}}\left(t^{n+1}\right) \cap \Omega_{\text{f}}\left(t^n\right)
$$
(A.12)

and

$$
\mathbf{u}^{n-1^*} = \mathbf{u}^{n-1} \quad \text{in } \Omega_{\text{f}}\left(t^{n+1}\right) \cap \Omega_{\text{f}}\left(t^{n-1}\right).
$$
(A.13)

The values of the fields $\mathbf{u}^{n^*}$ and $\mathbf{u}^{n-1^*}$ in $\Omega_{\text{f}}\left(t^{n+1}\right) \setminus \Omega_{\text{f}}(t^n)$ are approximated with a polynomial extrapolation.

With the velocity and pressure field of the fluid the hydrodynamic forces and torque and subsequently the acceleration of the particles is calculated. Especially for low Reynolds-numbers the effects of added damping due to the viscous shear stress at the particle surface become significant. To prevent instabilities and a diverging iteration process a method introduced by [31] is employed. The core idea is to make the dependency of the new particle state on the particle translational and rotational velocity in (A.7) visible. An expansion of the hydrodynamic forces and torque delivers [31]

$$
\begin{aligned}
_{k+1}F_p \left({}_{k+1}U, \, {}_{k+1}\dot{\mathbf{R}}_p, \, {}_{k+1}\dot{\varphi}_p \right) &\approx {}_{k+1}F_p \left({}_{k+1}U, \, , k\dot{\mathbf{R}}_p, k\dot{\varphi}_p \right) \\
&\quad - \boldsymbol{D}_{vv} \left({}_{k+1}\dot{\mathbf{R}}_p - {}_kF_p \right) \\
&\quad - \boldsymbol{D}_{vw} \left({}_{k+1}\dot{\varphi}_p - {}_k\dot{\varphi}_p \right)
\end{aligned}
$$
(A.14)

$$
\begin{aligned}
_{k+1}F_p \left({}_{k+1}U, \, {}_{k+1}\dot{\mathbf{R}}_p, \, {}_{k+1}\dot{\varphi}_p \right) &\approx {}_{k+1}T_p \left({}_{k+1}U, \, {}_k\dot{\mathbf{R}}_p, \, {}_k\dot{\mathbf{R}}_p \right) \\
&\quad - \boldsymbol{D}_{wv} \left({}_{k+1}\dot{\mathbf{R}}_p - {}_k\dot{\mathbf{R}}_p \right) \\
&\quad - D_{ww} \left({}_{k+1}\dot{\varphi}_p - {}_k\dot{\varphi}_p \right),
\end{aligned}
$$
(A.15)

where in two dimensions $\boldsymbol{D}_{vv}$ is a second order tensor, $\boldsymbol{D}_{vw}$ and $\boldsymbol{D}_{wv}$ are vectors and D_{ww} is a scalar. All four variables form a 3×3-matrix

$$\boldsymbol{D} = \begin{bmatrix} \boldsymbol{D}_{vv} & \boldsymbol{D}_{vw} \\ \boldsymbol{D}_{wv} & \boldsymbol{D}_{ww} \end{bmatrix}. \tag{A.16}$$

An approximation for the added damping tensor $\boldsymbol{D}$ is given in the aforementioned publication [31]. The tensor is calculated only one time in the begin of a simulation. In each time step after the update of the orientation angle the tensor is transformed with a rotation matrix

$$\boldsymbol{R} = \boldsymbol{A}\boldsymbol{A}^{\mathrm{T}}, \tag{A.17}$$

where A is a matrix containing the principle axis of inertia as column vectors. In each time step the added damping tensor is updated with

$$\boldsymbol{D}_{\alpha\varphi}^{n+1} = \boldsymbol{R}^{n+1}\boldsymbol{D}_{\alpha\varphi}^0 (\boldsymbol{R}^{n+1})^{\mathrm{T}}. \tag{A.18}$$

With the added damping tensors one obtains the following solver scheme for the particles. In a first step the hydrodynamic forces $k+1\mathbf{F}(k+1\mathbf{U}, k\dot{\chi}, k\dot{\varphi})$ and torque T $(k+1\mathbf{U}, k\dot{\chi}, k\dot{\varphi})$ are calculated with an integration over the level-set as given in (1) and (2). Added damping effects are then introduced by solving

$$\left\{ \begin{bmatrix} m_p\boldsymbol{E} & 0 \\ 0 & I_p \end{bmatrix} + \Delta t \zeta_{\mathrm{d}}\boldsymbol{D} \right\} \begin{bmatrix} _{k+1}\ddot{\mathbf{R}}_p \\ _{k+1}\dot{\varphi}_p \end{bmatrix} = \\ \begin{bmatrix} _{k+1}F_p \left(_{k+1}U, {}_k\dot{\mathbf{R}}_p, {}_k\dot{\varphi}_p \right) \\ _{k+1}F_p \left(_{k+1}U, {}_k\dot{\mathbf{R}}_p, {}_k\dot{\varphi}_p \right) \end{bmatrix} + \Delta t \zeta_{\mathrm{d}}\boldsymbol{D} \begin{bmatrix} _k\dot{\mathbf{R}}_p \\ _k\dot{\varphi}_p \end{bmatrix} \tag{A.19}$$

for the accelerations in the iteration $k+1$. To obtain the translational and rotational velocity of the particles the results have to be integrated in time. Following from equations (1) and (2) another temporal integration is necessary to obtain the position of the centre of mass and the orientation angle of each particle. Each of the four integration procedures is carried out using Keplers's rule

$$\psi^{n+1} = \psi^n + \frac{\Delta t}{6}\left(\dot{\psi}^{n+1} + 4\dot{\psi}^n + \dot{\psi}^{n-1} \right), \tag{A.20}$$

where ψ is the physical quantity in question.

A.2. Spatial discretization

The spatial discretization is based on the XDG method proposed by [19]. To simplify the notation in this chapter each quantity is part of the time step t^{n+1} and iteration-step $k+1$, hence, the reference to the time step and iteration can be omitted, i.e. $\mathbf{u} = k+1\mathbf{u}^{n+1}$. Only the fluid has to be discretized in space, whereas the particle solver has no spatial component. The fluid velocity field is approximated using polynomial functions of the order k. To satisfy the Ladyznskaja–Babuška–Brezzi condition ([32, 33]) the polynomial order of the pressure field is reduced by one $k' = k - 1$

$$(\mathbf{u}, p) \in \mathbb{P}_k(\phi, \Omega_h) \times \mathbb{P}_{k'}(\phi, \Omega_h) =: V_k, \tag{A.21}$$

where Ω_h is the domain of a single cell. The numerical grid consisting of H cells covers the complete domain $\Omega = \bigcup_{h=1}^H \Omega_h$ and the cells do not overlap. The polynomial space $\mathbb{P}_k$ with the order k is defined for each cells separately, i.e. there might be jumps at the cell boundaries. Jumps are represented by the jump operator $[\![\cdot]\!]$, which is defined as

$$[\![\mathbf{u}]\!](\mathbf{x}) = \lim_{\epsilon \searrow 0} [\mathbf{u}(\mathbf{x} + \epsilon\mathbf{n}_\Gamma) - \mathbf{u}(\mathbf{x} - \epsilon\mathbf{n}_\Gamma)]. \tag{A.22}$$

Furthermore, we define the average volume operator $\{\cdot\}$

$$\{\mathbf{u}\}(\mathbf{x}) = \frac{1}{2}\lim_{\epsilon \searrow 0}[\mathbf{u}(\mathbf{x} + \epsilon\mathbf{n}_\Gamma) + \mathbf{u}(\mathbf{x} - \epsilon\mathbf{n}_\Gamma)]. \tag{A.23}$$

Hence, one has to solve

$$\forall \ (\mathbf{v}, \tau) \in V_k \tag{A.24}$$

$$\left(\frac{3\mathbf{u}}{2\Delta t}, \mathbf{v} \right)_{\Omega_{\mathrm{f}}} + b(p, \mathbf{v}) - a(\mathbf{u}, \mathbf{v}) - b(\mathbf{u}, \tau) \\ = s(\mathbf{v}) + r(\mathbf{v}) + p(\mathbf{v}). \tag{A.25}$$

The first term is the temporal derivative, evaluated in the fluid domain Ω_{f}. The pressure gradient term is represented by $b(p, \mathbf{v})$. The third term $a(\mathbf{u}, \mathbf{v})$ is the viscous term and $b(\mathbf{u}, \tau)$ the continuity term. A detailed discussion of these terms can be found in [20]. In this paper we take a closer look to the viscous term $a(\mathbf{u}, \mathbf{v})$, because the active boundary condition is introduced via this term. The active stress in tangential direction on the active surface is implemented as a source term on the right-hand side of (A.25). Nevertheless, to ensure a slip-velocity at the surface the jump operators of the velocity $[\![\mathbf{u}]\!]|_{\Gamma_{\mathrm{ac}}}$ needs to vanish

$$[\![\mathbf{u}]\!]|_{\Gamma_{\mathrm{ac}}} = \lim_{\epsilon \searrow 0}\left[u_{\mathrm{t}}(\mathbf{x} + \epsilon\mathbf{n}_\Gamma) - u_{\mathrm{t}}|_{\Gamma_{\mathrm{ac}}} \right] = 0, \tag{A.26}$$

where $u_{\mathrm{t}} = \mathbf{u} \cdot \mathbf{t}_{\Gamma_{\mathrm{ac}}}$ is the fluid velocity in the direction of the tangential vector. Hence, one obtains for the viscosity term

$$a(\mathbf{u}, \mathbf{v}) = -\int_{\Omega_{\mathrm{f}}} \mu_{\mathrm{f}}\left(\nabla_h\mathbf{u} : \nabla_h\mathbf{v} + \nabla_h\mathbf{u}^{\mathrm{T}} : \nabla_h\mathbf{v} \right) \mathrm{d}V$$

$$+ \int_{\partial\Omega_{\mathrm{f}}\backslash\Gamma_{\mathrm{ac}}} \mu_{\mathrm{f}}\left\{ \nabla_h\mathbf{u} + \nabla_h\mathbf{u}^{\mathrm{T}} \right\}\mathbf{n}_{\partial\Omega_{\mathrm{f}}\backslash\Gamma_{\mathrm{ac}}} \cdot [\![\mathbf{v}]\!]\, \mathrm{d}S$$

$$+ \int_{\partial\Omega_{\mathrm{f}}\backslash\Gamma_{\mathrm{ac}}} \mu_{\mathrm{f}}\left\{ \nabla_h\mathbf{v} + \nabla_h\mathbf{v}^{\mathrm{T}} \right\}\mathbf{n}_{\partial\Omega_{\mathrm{f}}\backslash\Gamma_{\mathrm{ac}}} \cdot [\![\mathbf{u}]\!]\, \mathrm{d}S$$

$$- \int_{\partial\Omega_{\mathrm{f}}\backslash\Gamma_{\mathrm{ac}}} \eta\, [\![\mathbf{u}]\!] \cdot [\![\mathbf{v}]\!]\, \mathrm{d}S$$

$$+ \int_{\Gamma_{\mathrm{ac}}} \mu_{\mathrm{f}}\left(\mathbf{n}_{\Gamma_{\mathrm{ac}}} \cdot \left\{ \nabla_h\mathbf{u} + \nabla_h\mathbf{u}^{\mathrm{T}} \right\} \cdot \mathbf{n}_{\Gamma_{\mathrm{ac}}} \right)$$

$$\times \mathbf{n}_{\Gamma_{\mathrm{ac}}} \cdot [\![\mathbf{v}]\!]\, \mathrm{d}S$$

$$+ \int_{\Gamma_{\mathrm{ac}}} \mu_{\mathrm{f}}\left(\mathbf{n}_{\Gamma_{\mathrm{ac}}} \cdot \left\{ \nabla_h\mathbf{v} + \nabla_h\mathbf{v}^{\mathrm{T}} \right\} \cdot \mathbf{n}_{\Gamma_{\mathrm{ac}}} \right)$$

$$\mathbf{n}_{\Gamma_{\mathrm{ac}}} \cdot [\![\mathbf{u}]\!]\, \mathrm{d}S$$

$$- \int_{\Gamma_{\mathrm{ac}}} \eta\left(\mathbf{n}_{\Gamma_{\mathrm{ac}}} \cdot [\![\mathbf{u}]\!] \right)\left(\mathbf{n}_{\Gamma_{\mathrm{ac}}} \cdot [\![\mathbf{v}]\!] \right) \mathrm{d}S. \tag{A.27}$$

The parameter η is the penalty parameter, which is defined as [19]

$$\eta := \begin{cases} \mu_f \max\{\tilde{\eta}_{inn}, \tilde{\eta}_{out}\} & \text{on } \Gamma_{int} \\ \mu_f \tilde{\eta}_{inn} & \text{on } \partial\Omega_f \end{cases}, \qquad (A.28)$$

where Γ_{int} is an internal edge between two cells and $\tilde{\eta}_{inn}$ and $\tilde{\eta}_{out}$ are the local penalty parameters

$$\tilde{\eta} = \eta_0 k^2 G_h \qquad (A.29)$$

of the inner and outer cell at the internal edge. The factor $\eta_0 = 4$ in (A.29) is the local penalty factor, k is the polynomial degree and G_h a geometrical function arising from the shape of the cut cells [19].

On the right-hand side of (A.25) three different terms can be found. The first term $s(\mathbf{v})$ contains terms arising from the Dirichlet boundary conditions of the Stokes equation and the source term of the active boundary condition

$$\begin{aligned} s(\mathbf{v}) = &-\int_{\Gamma_D} \mathbf{u}_D \cdot \left(\nabla_h \mathbf{v} \mathbf{n}_{\Gamma_D} - \eta \mathbf{v}\right) \mathrm{d}S \\ &-\int_{\Gamma_{pa}} \mathbf{u} \cdot \left(\left(\nabla_h \mathbf{v} + \nabla_h \mathbf{v}^T\right) \mathbf{n}_{\Gamma_{pa}} - \eta \mathbf{v}\right) \mathrm{d}S \\ &-\int_{\Gamma_{ac}} \mu_f \left(\mathbf{n}_{\Gamma_{ac}} \cdot \left\{\nabla_h \mathbf{v} + \nabla_h \mathbf{v}^T\right\} \cdot \mathbf{n}_{\Gamma_{ac}}\right) \\ &\times \mathbf{n}_{\Gamma_{ac}} \cdot \mathbf{u} - \eta \left(\mathbf{n}_{\Gamma_{ac}} \cdot \mathbf{u}\right) \left(\mathbf{n}_{\Gamma_{ac}} \cdot \mathbf{v}\right) \mathrm{d}S \\ &-\int_{\Gamma_{ac}} \left(\boldsymbol{T}_{\Gamma_{ac}} \cdot \mathbf{f}_{ac}\right) \cdot \left(\boldsymbol{T}_{\Gamma_{ac}} \cdot [\![\mathbf{v}]\!]\right). \end{aligned} \qquad (A.30)$$

The second term $r(\mathbf{v})$ contains the Dirichlet terms of the continuity equation

$$r(\mathbf{v}) = \int_{\Gamma_D} \tau \mathbf{u}_{\Gamma_D} \cdot \mathbf{n}_{\Gamma_D} + \int_{\Gamma_p} \tau \mathbf{u}_{\Gamma_{pa}} \cdot \mathbf{n}_{\Gamma_{pa}}, \qquad (A.31)$$

which remained unchanged compared to passive particles.

The third term contains the additional terms of the temporal discretization (A.10)

$$p(\mathbf{v}) = -\int_{\Omega_f} \left(\frac{2\mathbf{u}^{n^*}}{\Delta t} - \frac{\mathbf{u}^{n-1^*}}{\Delta t}\right) \cdot \mathbf{v} \, \mathrm{d}V. \qquad (A.32)$$

A.3. Solver stability

To improve convergence we introduced Aitken-relaxation for the calculation of the forces. The principal idea of a relaxation method is the combination of the newly calculated solution with the solution of a previous iteration step

$$_{k+1}\mathbf{F}^{n+1} = {}_{k+1}\omega_{k+1}\mathbf{F}^* + \left(1 - {}_{k+1}\omega\right){}_k\mathbf{F}^{n+1}, \qquad (A.33)$$

where $_{k+1}\mathbf{F}^*$ is the unmodified solution of the current iteration. Instead of using a constant factor ω the Aitken-procedure calculates an optimal factor in each iteration step. A comparison between different relaxation-procedures and an outline of the principle idea of the Aitken-relaxation can be

found for example in [34]. For the purpose of calculating $_{k+1}\omega$ we write the particle force vectors into a single vector

$$\mathbf{F} = [\mathbf{F}_1, \dots, \mathbf{F}_N]. \qquad (A.34)$$

Furthermore, the residual vectors

$$_{k+1}R = k + 1\mathbf{F}^* - k\mathbf{F}^{n+1} \qquad (A.35)$$

and

$$_k\mathbf{r} = k\mathbf{F}^* - k - 1\mathbf{F}^{n+1} \qquad (A.36)$$

are introduced. The new relaxation coefficient is then calculated with [34]

$$k + 1\omega = -k\omega \frac{_k\mathbf{r} \cdot (k + 1\mathbf{r} - k\mathbf{r})}{\|k + 1\mathbf{r} - k\mathbf{r}\|^2}. \qquad (A.37)$$

To initialize the Aitken-relaxation it is necessary to calculate two iteration-steps with a static ω_c. The value can be chosen freely depending on the problem, however, it has been proven useful to use $\omega_c < 0.5$ for problems with multiple particles.

ORCID iDs

B Deußen ⬤ https://orcid.org/0000-0002-4444-3052
A Jayaram ⬤ https://orcid.org/0000-0001-6260-721X
F Kummer ⬤ https://orcid.org/0000-0002-2827-7576
Y Wang ⬤ https://orcid.org/0000-0002-5849-3755
T Speck ⬤ https://orcid.org/0000-0002-6357-1180
M Oberlack ⬤ https://orcid.org/0000-0002-5849-3755

References

[1] Lauga E and Powers T R 2009 *Rep. Prog. Phys.* **72** 096601
[2] Elgeti J, Winkler R G and Gompper G 2015 *Rep. Prog. Phys.* **78** 056601
[3] Purcell E M 1977 *Am. J. Phys.* **45** 3–11
[4] Dreyfus R, Baudry J, Roper M L, Fermigier M, Stone H A and Bibette J 2005 *Nature* **437** 862–5
[5] Shields C W and Velev O D 2017 *Chem* **3** 539–59
[6] Paxton W F, Baker P T, Kline T R, Wang Y, Mallouk T E and Sen A 2006 *J. Am. Chem. Soc.* **128** 14881–8
[7] Howse J R, Jones R A L, Ryan A J, Gough T, Vafabakhsh R and Golestanian R 2007 *Phys. Rev. Lett.* **99** 048102
[8] Niu R and Palberg T 2018 *Soft Matter* **14** 7554–68
[9] Masoud H and Shelley M J 2014 *Phys. Rev. Lett.* **112** 128304
[10] Shaebani M R, Wysocki A, Winkler R G, Gompper G and Rieger H 2020 *Nat. Rev. Phys.* **2** 181–99
[11] Lighthill M J 1952 *Commun. Pure Appl. Math.* **5** 109–18
[12] Kuron M, Stärk P, Burkard C, de Graaf J and Holm C 2019 *J. Chem. Phys.* **150** 144110
[13] Gompper G, Ihle T, Kroll D M and Winkler R G 2009 Multi-particle collision dynamics: a particle-based mesoscale simulation approach to the hydrodynamics of complex fluids *Advanced Computer Simulation Approaches for Soft Matter Sciences III* (Berlin: Springer) pp 1–87
[14] Howard M P, Panagiotopoulos A Z and Nikoubashman A 2018 *Comput. Phys. Commun.* **230** 10–20
[15] Hou T Y, Lowengrub J S and Shelley M J 2001 *J. Comput. Phys.* **169** 302–62
[16] Theers M, Westphal E, Qi K, Winkler R G and Gompper G 2018 *Soft Matter* **14** 8590–603

[17] Speck T 2019 *Phys. Rev.* E **99** 060602
[18] Clarke N, Gibbions N and Long D R 2020 *Soft Matter* **16** 3485–97
[19] Kummer F 2017 *Int. J. Numer. Methods Eng.* **109** 259–89
[20] Krause D and Kummer F 2017 *Comput. Fluids* **153** 118–29
[21] Kummer F, Weber J and Smuda M 2020 *Comput. Math. Appl.* **81** 237–57
[22] Kanevsky A, Shelley M J and Tornberg A-K 2010 *J. Comput. Phys.* **229** 958–77
[23] Saintillan D and Shelley M J 2013 *C. R. Phys.* **14** 497–517
[24] Jayaram A, Fischer A and Speck T 2020 *Phys. Rev.* E **101** 022602
[25] Drescher K, Dunkel J, Cisneros L H, Ganguly S and Goldstein R E 2011 *Proc. Natl Acad. Sci.* **108** 10940–5
[26] Hohenegger C and Shelley M 2011 *Dynamics of Complex Biofluids* vol 92 (Oxford: Oxford University Press)
[27] Batchelor G K 1970 *J. Fluid Mech.* **44** 419–40
[28] Costanzo A, Di Leonardo R, Ruocco G and Angelani L 2012 *J. Phys.: Condens. Matter* **24** 065101
[29] Lee C F 2013 *New J. Phys.* **15** 055007
[30] Schenk O, Gärtner K, Fichtner W and Stricker A 2001 *Future Gener. Comput. Syst.* **18** 69–78
[31] Banks J W, Henshaw W D, Schwendeman D W and Tang Q 2017 *J. Comput. Phys.* **343** 469–500
[32] Babuška I 1973 *Numer. Math.* **20** 179–92
[33] Brezzi F 1974 *ESAIM: Math. Modelling Numer. Anal.* **8** 129–51
[34] Birken P, Gleim T, Kuhl D and Meister A 2015 *Int. J. Numer. Methods Fluids* **79** 16–29